High Efficiency All-Dielectric Huygens Metasurfaces from the Ultraviolet to the Infrared

Journal:	*ACS Photonics*
Manuscript ID	ph-2017-013689.R2
Manuscript Type:	Article
Date Submitted by the Author:	21-Jan-2018
Complete List of Authors:	Ollanik, Adam; Tulane University, Physics and Engineering Physics Smith, Jake; Tulane University, Physics and Engineering Physics Belue, Mason; Tulane University, Physics and Engineering Physics; University of Arkansas, Biomedical Engineering Escarra, Matthew; Tulane University, Physics and Engineering Physics

High Efficiency All-Dielectric Huygens Metasurfaces from the Ultraviolet to the Infrared

Adam J. Ollanik[*†], Jake A. Smith[†], Mason J. Belue[†,‡], Matthew D. Escarra[†]*

[†]Department of Physics and Engineering Physics, Tulane University, New Orleans, Louisiana 70118, United States

[‡]Department of Biomedical Engineering, University of Arkansas, Fayetteville, Arkansas 72701, United States

KEYWORDS: subwavelength structures, nanophotonics, flat optics, Mie resonance, tunable metasurface, spectrum splitting, refractive index sensing

ABSTRACT: Conventional optics depend on the gradual accumulation of spatially dependent phase shifts imparted on light propagating through a medium to modify the wavefront of an incident beam. A similar effect may be obtained by the imposition of abrupt, discrete phase changes on a propagating wavefront over a sub-wavelength scale using photonic metasurfaces.

Highly efficient metasurfaces have applications ranging from conventional optics to high efficiency solar energy conversion, optical communications, and more. We present here the design, computational modeling, and experimental demonstration of all-dielectric transmissive Huygens metasurfaces exhibiting anomalous refraction, defined as the controlled deflection of light at an interface as a function of subwavelength nanostructures. These metasurfaces are comprised of dielectric, cylindrical elements, characterized by balanced electric and magnetic dipole resonances. For infrared wavelengths, optical efficiency of 91.3% is demonstrated computationally, and experimental efficiency of 63.6% is measured. Metasurfaces are designed and modeled in each of three experimentally realizable material systems, corresponding to incident wavelengths in the ultraviolet, visible, and infrared, all demonstrating high optical efficiency of at least 78%. A ground-up approach is presented that enables this design of highly efficient all-dielectric Huygens metasurfaces with non-zero phase gradients, in spite of difficulties due to strong inter-antenna coupling effects. Additionally, we computationally demonstrate a stacked metasurface device, capable of independent manipulation of four adjacent spectral bands, with mid-band optical efficiency as high as 55%. Taking advantage of the high sensitivity of this resonant dielectric Huygens metasurface approach, we discuss routes to the development of optical sensors and dynamically tunable metasurfaces.

Recent demonstrations of wavefront manipulation by the imposition of discrete phase shifts on a sub-wavelength scale, realized by flat, Huygens metasurfaces, have garnered significant interest in the optics community. These surfaces have shown potential for applications in optical devices such as lenses, holograms, spatial light modulators, and more. Despite successful demonstration of various devices[1–3], resonant plasmonic metasurfaces are plagued by intrinsic absorption losses[4–6]. All-dielectric platforms offer an alternative route to gradient metasurface optics with high efficiency[7]. To date, three distinct styles of all-dielectric metasurfaces have emerged. The first employs a dominant electrical resonance in asymmetric nanobeams to locally rotate polarization and create a geometric (Pancharatnam-Berry) phase shift[8–10]. Highly efficient (as high as 86% demonstrated experimentally for lensing)[11] transmissive PB metasurfaces have been demonstrated with anomalous properties in the visible and infrared (IR), and minimal inter-element coupling has even enabled the development of interleaved devices[12], but the technique is inherently constricted to circularly polarized incident light. A second approach utilizes high aspect ratio nanoposts which function as truncated waveguides supporting low quality factor Fabry-Perót resonances[13]. Propagation phase is modulated by the effective refractive index of nanoposts, dependent on the geometrical parameters of the post within a unit cell. Negligible interaction with neighboring posts and tolerance to fabrication error make this a robust approach, and highly efficient devices (as high as 77% demonstrated experimentally for anomalous refraction, and 83% for lensing)[13,14] have been demonstrated with anomalous properties for visible and infrared light[15–17]. The high aspect ratio of nanoposts may imply practical fabrication limitations, especially for devices designed for shorter wavelengths[18]. The third approach, and the one described in this paper, utilizes low aspect ratio nanocylinders that use spectrally overlapping electric and magnetic dipole Mie-type resonances to locally control the propagation phase of incident light[19–21]. These nanocylinder elements may be described as Huygens source nanoantennas[22]. Several demonstrations of this approach have been reported, including holograms[23,24] (experimental efficiency as high as 40%)[24], as well as gradient surfaces for visible and infrared light[25,26] (experimental efficiency as high as 45% for anomalous refraction)[25]. Contributing to previous shortcomings of this method is strong inter-element coupling, which greatly enhances the difficulty of designing gradient metasurfaces. For PB and Fabry-Perót approaches, phase delay elements may be independently designed, added to an element library, and later placed in a complex metasurface to impart the desired local phase shift, with little concern given to the geometry of adjacent elements[27]. Dielectric Huygens source nanoantennas must always be considered in the context of an array, taking into account the geometry of neighboring elements. To mitigate this constraint, and aid in the development of highly efficient gradient metasurfaces, we employ several specialized design techniques in this work. Utilizing these techniques, we demonstrate transmissive metasurfaces with highly efficient anomalous refraction for incident wavelengths in the IR, visible, and ultraviolet (UV) portions of the optical spectrum. The highly resonant nature of these nanoantenna elements makes this platform especially sensitive to small changes in either geometry or intrinsic material parameters. Although this decreases fabrication tolerance, this sensitivity is useful for a number of applications. Dielectric Huygens metasurfaces, defined by spectrally overlapping electric and magnetic dipole resonances, are well-suited for dynamic uses, with promising applications in optical sensing[28,29] as well as actively tunable devices[30–32]. High optical efficiency, even for UV wavelengths, combined with a relatively low height profile and ease of fabrication make this platform a promising approach for metasurface optical devices.

A Huygens metasurface is designed to impose an arbitrary phase profile on an incident beam, thereby shaping the outgoing beam to serve an intended purpose. Such a phased array metasurface requires a set of nanoantenna elements spanning a 2π range of phase shifts with equal amplitude emittance. In this work, we focus on the development of gradient metasurfaces demonstrating anomalous refraction in accordance with the generalized Snell's law[1,33]. Symmetry and periodicity allow a large-scale metasurface to be computationally modeled using the finite element method, enabling direct comparison between modeled and experimental results.

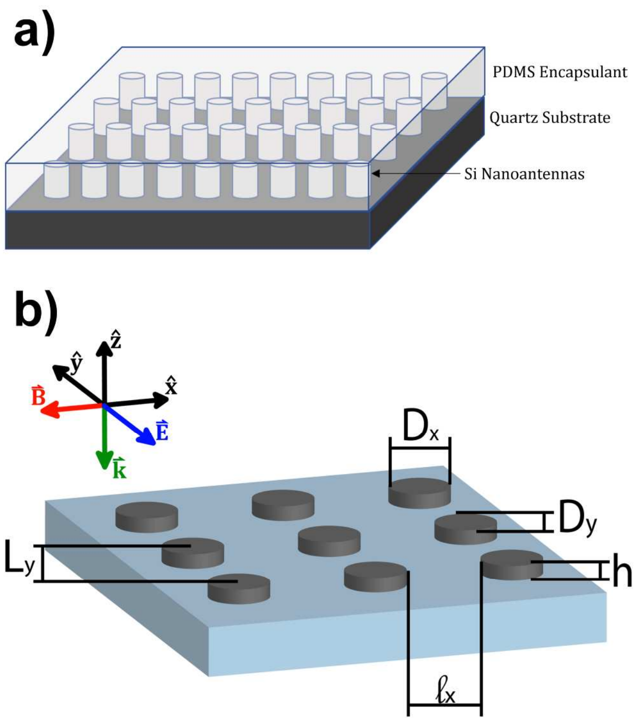

Figure 1. a) Diagram of all-dielectric Huygens metasurface, with the material system experimentally demonstrated in this paper. b) Important array parameters: Unit cell spacing, $L_{y,}$ in the direction of electric field polarization; edge-to-edge spacing, l_x, in the direction of magnetic field polarization; nanoantenna height, h, and elliptical nanoantenna diameter in the direction of electric and magnetic fields, D_y and D_x, respectively.

Material selection is critical to the development of highly efficient metasurface optics[18]. The metasurfaces described here have three material domains: substrate, nanoantenna elements, and encapsulant (figure 1a). All three materials must be minimally absorbing in the relevant spectrum. The nanoantenna material should have a high refractive index, while the substrate and encapsulant should be low index materials. Normally, the substrate and encapsulant are chosen to have similar index in order to facilitate high transmittance. Here, three metasurfaces comprised of three material systems, chosen respectively for IR, visible, and UV light, are discussed and evaluated to demonstrate the versatility of the dielectric Huygens metasurface approach. For all three, polydimethylsiloxane (PDMS) is chosen as the encapsulant. PDMS is index- and process-compatible with most low-index substrates, and serves the additional purpose of creating a flat surface, regardless of the encapsulated nanostructure, which is useful for further optical integration including multi-layer metasurfaces. Fused quartz is chosen as substrate for IR and visible metasurfaces due to its practicality, and magnesium fluoride for UV metasurfaces in order to demonstrate material versatility and minimize refractive index of the substrate. For IR metasurfaces, amorphous silicon is chosen as the nanoantenna material. Silicon is an ideal choice due to its high index contrast with the substrate and encapsulant, lack of absorption, and standardized fabrication processes. For UV metasurfaces, titanium dioxide is chosen for its high index and low absorption at short wavelengths. Although TiO_2 could be used for visible wavelengths as well, gallium phosphide is used here to again demonstrate versatility of material selection and to increase the refractive index of nanoantennas.

The first step in the design of a transmissive gradient Huygens metasurface is the design of a periodic array of homogeneous nanoantenna elements exhibiting overlapping electric and magnetic dipole resonances at the intended incident wavelength. Regardless of chosen material, the resonant wavelength is broadly tunable through adjustment of the geometric parameters of nanoantenna elements. For circular cylindrical resonators, the electric resonance is more sensitive to diameter than the magnetic resonance, as shown in figures 2d and 2e. This allows the cylinder diameter to be tuned so that the two resonances occur at the same wavelength. For a given cylinder height, there is a single cylinder diameter, and wavelength, at which resonance overlap occurs. Due to strong inter-antenna coupling, spacing between elements must be carefully adjusted to effectively suppress back scattering and maximize transmittance. As a design guideline, the geometric parameters of a highly transmissive resonant array are as follows, as a fraction of the incident wavelength in vacuum: height: 0.16; diameter: 0.35; unit cell: 0.57. These parameters were calculated for silicon nanoantennas and need slight adjustment to match other material systems.

Due to significant inter-antenna interaction, all modeling must be done in the context of an array. Periodic boundary conditions are used to simulate an infinitely extending, homogeneous array of nanoantenna elements. As cylinder diameter is varied about the resonance, with all other parameters held constant, a 2π range of phase shifts is obtained (see figure 2c). Construction of a rudimentary gradient metasurface is at this point possible. A series of elements is chosen, spanning the 2π phase shift range in equal increments, and aligned in an array. Unfortunately, inter-element coupling causes these elements to perform differently in a gradient array than a homogeneous one, and performance of the resulting gradient metasurface is un-optimized, reaching only 48% efficiency. The creation of a high-performing gradient metasurface requires the mitigation of these effects. We note that element performance with regards to coupling effects is most significantly modified by changes in the edge-to-edge spacing of elements in the direction of the magnetic field. We fix incident polarization such that the magnetic field is aligned in the direction of phase gradient, and electric field in the direction of constant phase (figure 1b). We further apply a design constraint that the edge-to-edge element spacing in the direction of phase gradient be fixed, while unit cell periodicity is maintained along the other dimension (figure 1b).

Design improvements are applied to nanoantenna elements as well. Allowing cylinders to take elliptical form greatly broadens the space of useful antenna elements. Although any elements spanning a 2π phase shift range with high transmittance may be selected, we may conveniently choose a high-quality set of elements with equal x-diameters and varied y-diameters, as shown in Figures 2a and 2b. This set of elements is favorable for more fundamental reasons as well; across this set, the electric and magnetic dipole resonances shift at the same rate (figure 2f), in sharp contrast to sets comprised of circular nanoantenna elements (figures 2d and 2e). Elements selected from this set may be placed in an array to form a gradient metasurface. Without any further steps, metasurfaces demonstrating anomalous refraction efficiency as high as 78% may be routinely designed. The angle of anomalous refraction is dependent on the periodicity of the array, as described by the generalized Snell's law[1], here modified to match the specific design: $\theta_t = \sin^{-1}\left(\frac{1}{n_t}\left(\frac{\lambda_0}{W_p} + (\sin\theta_i)n_i\right)\right)$, where θ_t and θ_i are the transmitted and incident angles, respectively; n_t and n_i are the refractive index of the substrate and encapsulant, respectively; λ_0 is the incident wavelength in vacuum, and W_p is the periodicity of the array, defined as $W_p = m * l_x + \sum_{i=1}^{m} D_{x,i}$, where m is the number of elements in the array, l_x is the edge-to-edge spacing in the dimension of phase gradient, and $D_{x,i}$ are the diameters of nanoantenna elements in the direction of phase gradient. Since antenna edge-to-edge spacing in the phase gradient direction is held constant and antenna diameter is mandated by the desired phase shift, the periodicity, and therefore intended deflection angle, is determined by the number of unique elements in the array. As a general rule, arrays with more elements, and shallower phase gradient, achieve higher efficiency at a smaller angle of deflection. Arrays with very few elements, and large deflection angles, are more difficult to achieve high efficiency with. We chose to use 9-element arrays with a designed deflection angle of ~8°, as a compromise between high efficiency and significant deflection angle.

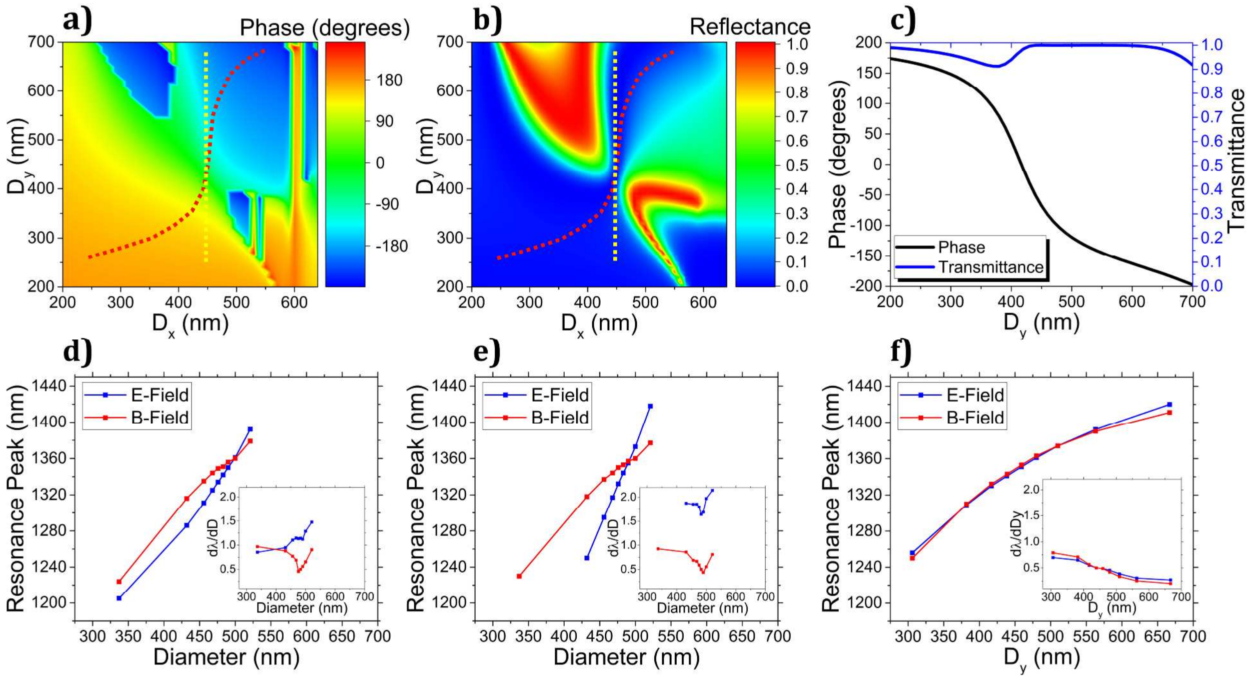

Figure 2. a) Phase and b) reflectance of homogeneous arrays of nanoantenna elements with varying elliptical diameters. The red dashed line denotes an arbitrary selection of elements covering a 2π phase shift range with near unity transmittance. The yellow dashed line depicts the set of nanoantenna elements with fixed x-diameter, as chosen in this work. c) Phase and transmittance for the set of nanoantenna elements depicted by the yellow dashed line in a), b). (d-f) Shifting electric and magnetic dipole resonances with respect to nanoantenna diameter for three array configurations: d) circular nanoantennas with fixed unit cell spacing in both dimensions, e) circular nanoantennas with fixed x- edge-to-edge spacing and y- unit cell spacing, and f) elliptical nanoantennas with fixed x- diameter, x- edge-to-edge spacing, and y- unit cell spacing. Insets show rate of resonance shift.

To further improve results, a straight forward computational optimization is performed. The optimization makes small changes, on the order of 2%, to the height and diameters of elements, and the two spacing parameters of the array. The heights of cylinders are of course constrained to be equal. This optimization is intended to correct both for human inaccuracy in the original design and small differences in element function in the gradient array as compared to the homogenous arrays in which they are independently modeled. The Nelder-Mead simplex method is used, chosen for its simplicity and speed, as the initial array to be optimized is already high-performing[34]. This optimization further increases optical efficiency from 78% to nearly 90% for IR metasurfaces, as an example. Optical efficiency is defined as the intensity of anomalously refracted light exiting the antenna array divided by the intensity of light incident on the antenna array. Reflection at the air/encapsulant and substrate/air interfaces are not included in simulations.

Using these design methods, three gradient metasurfaces were designed and modeled using the three distinct material systems described above. Amorphous silicon nanoantennas were used for a metasurface designed for IR light (1340nm), gallium phosphide for visible light (610nm), and rutile titanium dioxide for UV light (378nm). For the IR array, nanocylinders have a height of 220nm and diameters between 300nm and 700nm. For the visible array, nanocylinders have a height of 110nm and diameters between 140nm and 310nm. For the ultraviolet array, nanocylinders have a height of 60nm and diameters between 85nm and 200nm. For normally incident light, at the designed wavelength and polarization, optical efficiency of 88% was achieved for the IR array, 78% for the visible array, and 78% for the UV array, as shown in Figure 3a. Parameters for the three metasurface arrays represented in figure 3a can be found in the Supporting Information (Tables S1, S2, and S3). To the authors' knowledge, this is the first reported UV metasurface featuring spectrally overlapping electric and magnetic dipole resonances[4,35–37].

The IR metasurface was further evaluated for incident angle, varied in the direction of the phase gradient (Figure 3b), and wavelength (Figure 3c). An effective bandwidth of ~80nm, or ~6% of the incident wavelength, was observed. Within this band, incident light is deflected at the designed angle; incident light outside the band is transmitted normally, with minimal interaction with the metasurface. An acceptance angle range of ~35° (+15°/-20°) is observed, shifted ~5° in the direction of the deflected angle. Within that range, anomalous refraction is efficient and closely matches the generalized Snell's law. Relatedly, optimal performance for the array occurs at an incident angle of 4.5°. In recent related work for homogenous Huygens metasurfaces, the effects of a spectrally adjacent third resonant mode have been discussed to explain significant drop in performance at higher incidence angles[38]. This antisymmetric mode is observed in our metasurfaces at small incidence angles and results in several reflectance peaks. The effects of these reflectance peaks are noticeable in our nine element anomalously refracting array and are at least partially responsible for the drop in efficiency at higher incidence angles. In Figures 3d-f, these characteristic reflectance peaks can be seen at higher incidence angles for homogenous arrays composed of each of the nine elements making up the anomalously refracting array discussed in Figure 3b (plotted for incidence angles of 0°, 4°, and 8°, in Fig. 3d-f respectively). As the reflectance peaks are spectrally shifted for each of the several elements in the phased array, at any given wavelength only some elements exhibit reduced transmittance, allowing the metasurface as a whole to continue functioning with relatively high efficiency and greatly reduced incidence angle sensitivity compared to previous results[38].

Finally, we note that these arrays are polarization sensitive, due to the asymmetric shape and spacing of cylindrical elements. At cross-polarization, efficiency drops significantly (see Figure

5c). Note that this polarization sensitivity is not a fundamental constraint and may be overcome through use of designs with approximate rotational symmetry[24].

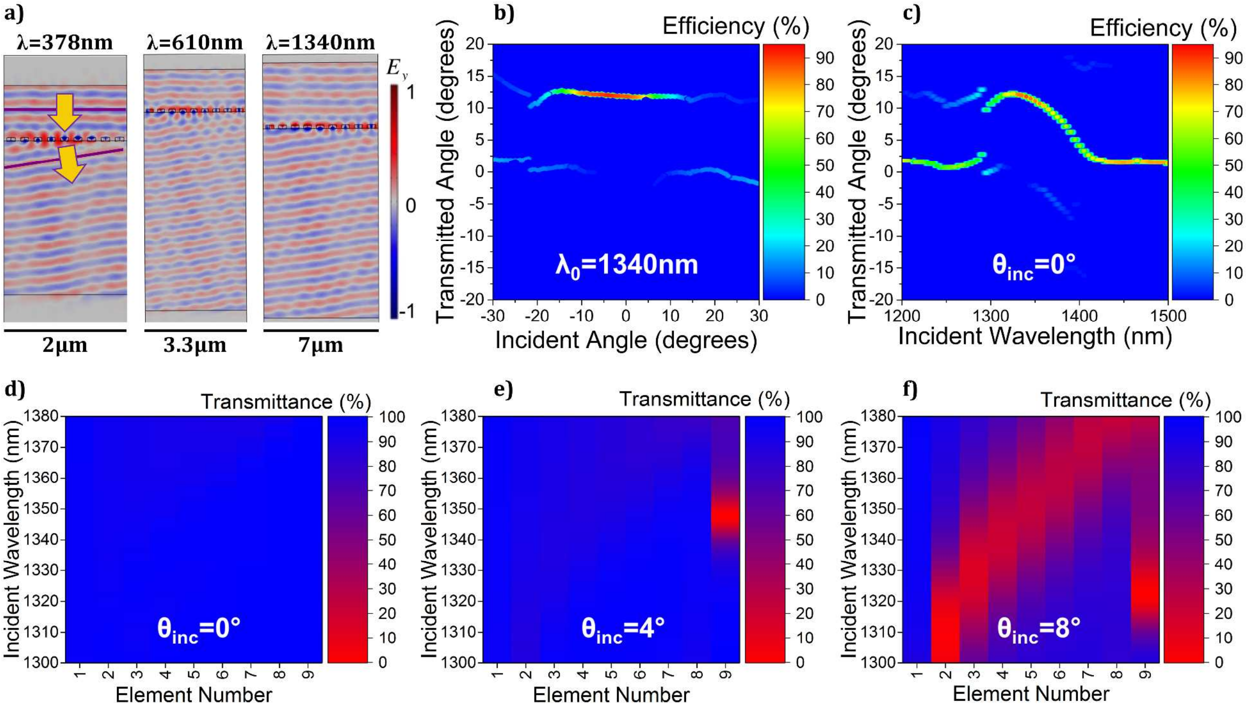

Figure 3. a) Modeling results of three metasurfaces demonstrating anomalous refraction for different materials and spectral bands. Depicted is the electric field intensity in the y-axis (into the page). A plane wave normally incident from the top of the model is transmitted at a deflected angle. Left is designed for UV light of λ_0=378nm, using TiO_2 nanoantennas and MgF_2 substrate; optical efficiency at normal incidence is 78%. Center is designed for visible light of λ_0=610nm, using GaP nanoantennas and fused quartz substrate; optical efficiency at normal incidence is 78%. Right is designed for IR light of λ_0=1340nm, using Si nanoantennas and fused quartz substrate, as demonstrated experimentally; optical efficiency at normal incidence is 88%. b) Modeled efficiency and transmitted angle of the λ_0=1340nm array vs. incident angle. Maximum optical efficiency is found to be 91.3% at an incident angle of -4.5°. c) Modeled efficiency and

transmitted angle for the λ_0=1340nm array vs. incident wavelength. An effective bandwidth of ~80nm is observed. For (b) and (c), Snell's law at the substrate/air interface has been applied to computational results to facilitate comparison with experimental results in Figure 5. d-f) Each of the nine elements from the array discussed in a-c is modeled as a homogenous array, and transmittance vs. wavelength is plotted for each of those nine homogenous arrays for incidence angles of 0°, 4°, and 8° respectively. The incident angle range reflects that in which anomalous refraction is observed. The average transmittance at λ_0=1340nm is 98% at 0°, 89% at 4°, and 53% at 8°.

These metasurfaces are fabricated using standard nanofabrication procedures, with antenna material deposition, lithography, mask deposition, and anisotropic etching as the four critical steps. Required lithographic resolution falls within the capabilities of deep UV and nanoimprint technology[39,40]. The low height profile of these nanoantenna elements makes the dielectric Huygens metasurface platform particularly appealing from a fabrication perspective. Due to resolution limitations of our current equipment, we chose to demonstrate these metasurfaces experimentally in the IR spectrum, using amorphous silicon nanoantenna elements. Silicon is deposited using electron beam evaporation. Electron beam lithography (EBL) is performed, using an SEM outfitted with the NPGS lithography package. PMMA A2 (Microchem) positive resist is used, with cold development in MIBK:IPA 1:3 solution at -14°C used to improve resolution and repeatability of results[41]. A thin alumina etch mask is deposited, again using electron beam evaporation. Reactive ion etching is performed using C_4F_8 and SF_6 at 57sccm and 33sccm, respectively[42], at a pressure of 10mT; ICP power is set to 1000W and RIE power to 110W; etch rate is measured to be slightly more than 1nm/s, with a high degree of anisotropy. Both etch mask and substrate are largely impervious to the etch. The etch mask is removed in a solution of $NH_4OH:H_2O_2:H_2O$ 1:1:3 at 80°C; this wet etch has a negligible effect on the nanoantenna elements and substrate. SEM images of a fabricated array are shown in figure 4. Finally, PDMS encapsulant is applied by spin coating and cured at 180°C.

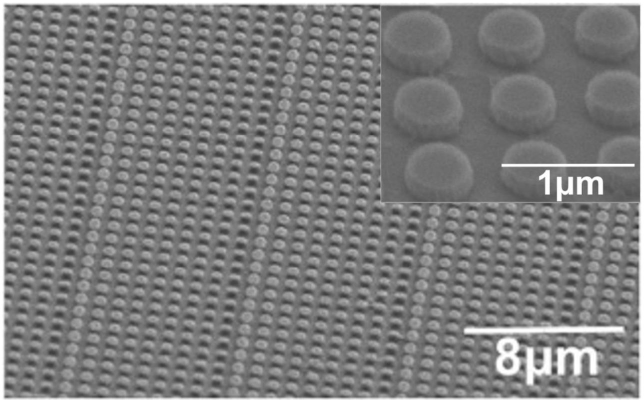

Figure 4. Electron microscopy image of fabricated 9-element metasurface composed of silicon nanoantennas. Inset shows a higher magnification image, depicting high fidelity of elements meeting design requirements for anisotropy, geometry, and roughness.

Fabricated metasurfaces are characterized using a motorized, 8-axis goniospectrometer (x, y, z, and rotation control for both sample and detector). A Fianium supercontinuum source in combination with an LLTF tunable narrow-bandpass filter provides a finely tunable incident wavelength. A photodetector, revolving about the metasurface sample, spatially characterizes the transmitted light. Incident light is fully focused inside the metasurface area using a 5X objective. A metasurface designed for 1340nm incident light was fabricated and characterized, for direct comparison with modeled results in Figures 5a, 5b, and 5c. A maximum metasurface optical efficiency of 63.6% was measured at an incident angle of 4°. Spectral bandwidth was measured to be ~80nm, in accordance with modeling results. The measured acceptance angle range is in agreement with modeling results as well, including the ~5° shift towards the direction of anomalous refraction. At normal incidence, efficiency is measured to be 57% at the designed polarization and 23% at the cross polarization. Efficiency here is defined as the intensity of light measured at the angle of anomalous refraction divided by normally transmitted intensity through the encapsulant and substrate at a location adjacent to the metasurface sample. The lower efficiency of the fabricated device as compared to modeling results is attributed most significantly to fabrication error. Dimensions of nanoantenna elements were measured to vary from designed parameters with a 2σ deviation of about 8%. To the authors' knowledge, these results indicate the best yet reported efficiencies (both modeled and experimental) for phase gradient metasurfaces featuring spectrally overlapping electric and magnetic dipole resonances.

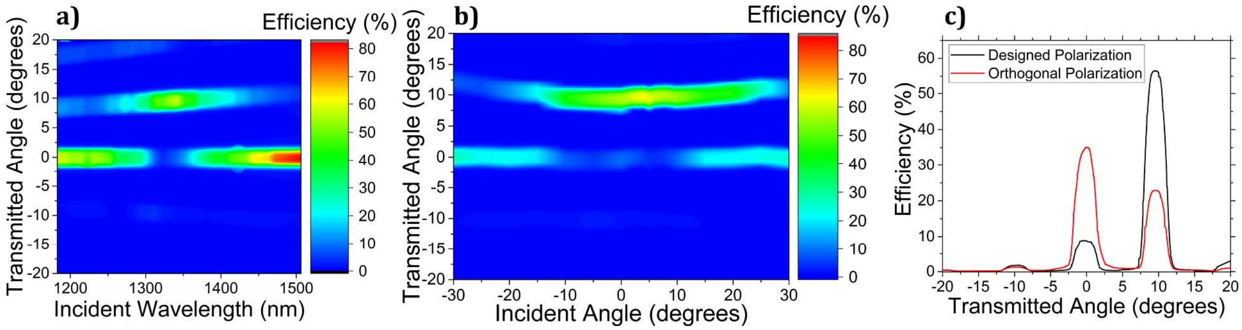

Figure 5. Experimental measurements of fabricated metasurface designed for λ_0=1340nm using Si nanoantenna elements, PDMS encapsulant, and fused quartz substrate. a) Transmitted angle and efficiency vs. incident wavelength. A bandwidth of ~80nm is observed. b) Transmitted angle and efficiency vs. incident angle. Maximum optical efficiency is measured to be 63.6% at an incident angle of 4°. c) Transmitted angle and efficiency for the designed and orthogonal polarizations. A significant decrease in optical efficiency is observed for the orthogonal polarization.

Due to the well-defined bandwidth, resulting from the resonant nature of dielectric Huygens metasurface elements, it is possible to construct a multi-layer spectrum splitting device in which each layer independently manipulates a selected band of light with minimal cross-talk. A three-layer metasurface device capable of 4-way spectrum splitting is illustrated in Figure 6a and demonstrated computationally in Figure 6b, showing independent anomalous refraction of four distinct bands, from 1100nm to 1500nm, with mid-band optical efficiency as high as 55%. Metasurface array parameters, individual performance for the three arrays making up the multi-layer device, and details of the mid-band performance for the composite stacked device can be found in the Supporting Information (Tables S4, S5, S6, and S7). Anomalous refraction angle ranges from 8° to -4°. For this work, each layer of the device was separately designed; efficiency could be significantly enhanced through optimization. Although multiplexing of anomalous refraction is demonstrated here, other optical effects such as lensing and hologram formation could be equivalently assembled into a multiplexed optical structure with minimal crosstalk due to the narrow, resonant spectral bands of interaction in each metasurface. This device is possible to fabricate using the same techniques described above, with each layer fabricated on top of the last[43], and with PDMS encapsulant between successive layers. An alternative route to fabrication would involve lifting off nanocylinders embedded in the PDMS encapsulant[32,44], and mechanically aligning subsequent layers. Single devices able to independently manipulate the wavefront of various incident bands may have useful applications in optical communications, solar energy collection[45,46], display technology, and more.

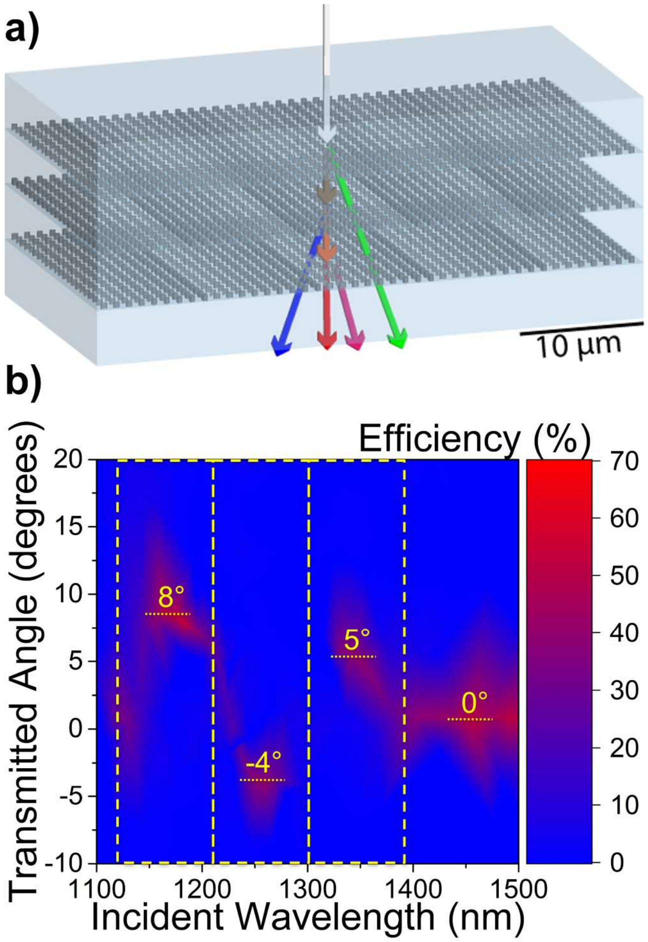

Figure 6. a) Diagram of modeled spectrum splitting device. Three anomalously refracting metasurface layers separate incident light into four bands traveling in different directions, with independent control over each. b) Modeling results of the spectrum splitting device depicted in (a). Mid-band optical efficiency reaches as high as 55%.

The resonance of dielectric Huygens sources is very sensitive to material properties of nanoantennas and the encompassing medium, as well as the geometry of the resonators and the array they are placed in[30–32,47]. The optical response of a metasurface based on these principles is therefore sensitive as well. In order to evaluate this sensitivity, and inform future work towards the development of tunable metasurfaces, we computationally conducted a survey of various tunable parameters. This survey is done using an all-dielectric homogenous metasurface array of silicon nanoantenna elements immersed in SiO_2 encapsulant and substrate, designed for λ_0=1340nm. The array was designed to be highly reflective, with emitted phase chosen to suppress forward scattering; array parameters are as follows: l_x=l_y=331nm, D=420nm, h=260nm, antenna refractive index=3.511 (silicon at λ_0=1340nm), encapsulant refractive index=1.3992 (PDMS at λ_0=1340nm), substrate refractive index=1.4465 (SiO_2 at λ_0=1340nm). Variation of array parameters disrupt this effect, causing the surface to become transmissive. Quantitative results are shown in Figure 7 and Table 1, showing dramatic tuning (>80% transmittance modulation) for as little as 3.8% shift in an array parameter. The sensitivity of the dielectric Huygens metasurface platform is of great value, as it may lead to the realization of dynamically tunable metasurfaces and the development of precise optical sensors at the micron scale.

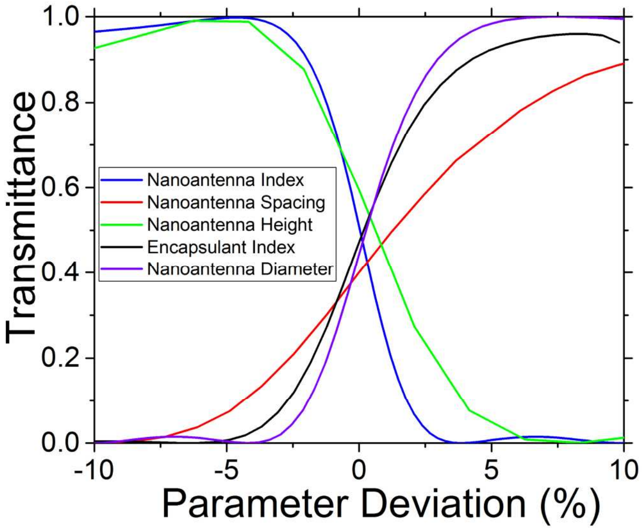

Figure 7. Modeling results depicting modulated transmittance through a homogenous metasurface in response to variation of geometric and material parameters. Results are based around a material system using circular, cylindrical Si nanoantenna elements and SiO_2 encapsulant and substrate, where absorption is negligible for incident light of λ_0=1340nm. '0' parameter deviation denotes the parameter value at peak sensitivity; these points are:

l_x=l_y=410nm, D=472nm, h=240nm, antenna index=3.37, and encapsulant index=1.63. Note that nanoantenna edge-to-edge spacing, l_x and l_y, is the varied spacing parameter.

Table 1. Metasurface Sensitivity to Tuning

	nanoantenna height	nanoantenna diameter	edge-to-edge spacing	nanoantenna refractive index	encapsulant refractive index
sensitivity[a]	14.5%	22.0%	7.9%	27.4%	16.4%
range[b]	6.4%	4.7%	15.0%	3.8%	6.7%

In summary, the dielectric Huygens metasurface platform shows remarkable promise as a route to practical metasurfaces. The low profile of nanoantenna elements allows for easier manufacturing than alternative designs, while maintaining similar high efficiency performance. Here we show modeled efficiency as high as 91% with experimental efficiency of 64%, demonstrating that dual-dipole, Mie-type metasurfaces can achieve efficiencies on par with other types of dielectric metasurfaces. Inter-element coupling makes gradient metasurface design more difficult, but these effects may be mitigated through application of careful design rules, as outlined here. Additionally, the resonant nature of this platform makes it uniquely advantageous for multiplexing and dynamically tunable applications in optical communications, solar energy conversion, display technologies, micron-scale sensors, and more.

---

[a] Sensitivity given as % transmittance modulation in response to 1% change in parameter value

[b] Range is defined as the parameter variation required for 80% transmittance modulation

ASSOCIATED CONTENT

Supporting Information.

The following files are available free of charge.

Array parameters for the 6 metasurfaces described in this paper; specifics regarding the individual performance of the 3 metasurfaces that make up the stacked device depicted in figure 6; specifics regarding the mid-band performance for the composite stacked device depicted in figure 6 (PDF).

AUTHOR INFORMATION

Corresponding Author

*E-mail: aollanik@gmail.com

Author Contributions

The manuscript was written through contributions of all authors. All authors have given approval to the final version of the manuscript. A.O. and M.E. proposed the idea developed in this work. A.O. made the design and performed the numerical simulations. J.S. assisted with analysis of the modeled results and with computational optimization. A.O. did the fabrication of the samples. A.O. and M.B. performed the optical characterization of the samples. A.O. and M.E. wrote the paper. M.E. supervised this work.

ACKNOWLEDGEMENT

The majority of this work was supported by the Louisiana Board of Regents Support Fund (Contract#: LEQSF(2014-17)-RD-A-08). Experimental validation was supported by the National Science Foundation DMR-1654765; REU student Mason Belue was also supported by DMR-1460637. The authors thank Matt Fortuna, Ben Lewson, and Max Woody for their contributions towards the development of an optical characterization set up used in this work, and Nick Farrar-Foley for his early contributions towards development of a relevant fabrication process. This research was supported in part using high performance computing (HPC) resources and services provided by Technology Services at Tulane University, New Orleans, LA.

REFERENCES

(1) Yu, N.; Genevet, P.; Kats, M. A.; Aieta, F.; Tetienne, J.-P.; Capasso, F.; Gaburro, Z. Light Propagation with Phase Discontinuities: Generalized Laws of Reflection and Refraction. *Science (80-.).* **2011**, *334* (21), 333–337 DOI: 10.1126/science.1210713.

(2) Kim, M.; Wong, A. M. H.; Eleftheriades, G. V. Optical Huygens' Metasurfaces with Independent Control of the Magnitude and Phase of the Local Reflection Coefficients. *Phys. Rev. X* **2014**, *4* (41042), 1–11 DOI: 10.1103/PhysRevX.4.041042.

(3) Ni, X.; Kildishev, A. V.; Shalaev, V. M. Metasurface Holograms for Visible Light. *Nat. Commun.* **2013**, *4*, 1–6 DOI: 10.1038/ncomms3807.

(4) Yu, N.; Capasso, F. Flat Optics with Designer Metasurfaces. *Nat. Mater.* **2014**, *13*, 139–150 DOI: 10.1038/nmat3839.

(5) Zhao, Y.; Liu, X.-X.; Alù, A. Recent Advances on Optical Metasurfaces. *J. Opt.* **2014**, *16* (12), 1–14 DOI: 10.1088/2040-8978/16/12/123001.

(6) Naik, G. V.; Shalaev, V. M.; Boltasseva, A. Alternative Plasmonic Materials: Beyond Gold and Silver. *Adv. Mater.* **2013**, *25*, 3264–3294 DOI: 10.1002/adma.201205076.

(7) Jahani, S.; Jacob, Z. All-Dielectric Metamaterials. *Nat. Nanotechnol.* **2016**, *11*, 23–36 DOI: 10.1038/nnano.2015.304.

(8) Hasman, E.; Kleiner, V.; Biener, G.; Niv, A. Polarization Dependent Focusing Lens by Use of Quantized Pancharatnam–Berry Phase Diffractive Optics. *Cit. Appl. Phys. Lett. Appl. Phys. Lett. Appl. Phys. Lett. Appl. Phys. Lett. Appl. Phys. Lett. Appl. Phys. Lett* **2003**, *82* (79), 241104–203505 DOI: 10.1063/1.1539300.

(9) Lin, D.; Fan, P.; Hasman, E.; Brongersma, M. L. Dielectric Gradient Metasurface Optical Elements. *Science (80-.).* **2014**, *345* (6194), 298–302 DOI: 10.1126/science.1253213.

(10) Devlin, R. C.; Khorasaninejad, M.; Chen, W.-T.; Oh, J.; Capasso, F. Broadband High-Efficiency Dielectric Metasurfaces for the Visible Spectrum. *PNAS* **2016**, *113* (38), 10473–10478 DOI: 10.1073/pnas.1611740113.

(11) Khorasaninejad, M.; Chen, W. T.; Devlin, R. C.; Oh, J.; Zhu, A. Y.; Capasso, F. Metalenses at Visible Wavelengths: Diffraction-Limited Focusing and Subwavelength Resolution Imaging. *Science (80-.).* **2016**, *352* (6290), 1190–1194 DOI: 10.1126/science.aaf6644.

(12) Maguid, E.; Yulevich, I.; Yannai, M.; Kleiner, V.; L Brongersma, M.; Hasman, E. Multifunctional Interleaved Geometric-Phase Dielectric Metasurfaces. *Light Sci. Appl.* **2017**, *6* (8), 1–7 DOI: 10.1038/lsa.2017.27.

(13) Arbabi, A.; Horie, Y.; Bagheri, M.; Faraon, A. Dielectric Metasurfaces for Complete Control of Phase and Polarization with Subwavelength Spatial Resolution and High Transmission. *Nat. Nanotechnol.* **2014**, *10* (1038), 937–944 DOI: 10.1038/nnano.2015.186.

(14) Zhou, Z.; Li, J.; Su, R.; Yao, B.; Fang, H.; Li, K.; Zhou, L.; Liu, J.; Stellinga, D.; Reardon,

C. P.; Krauss, T. F.; Wang, X. Efficient Silicon Metasurfaces for Visible Light. *ACS Photonics* **2017**, *4*, 544–551 DOI: 10.1021/acsphotonics.6b00740.

(15) Arbabi, E.; Arbabi, A.; Mahsa Kamali, S.; Horie, Y.; Faraon, A. High Efficiency Double-Wavelength Dielectric Metasurface Lenses with Dichroic Birefringent Meta-Atoms. *Opt. Express* **2015**, *3* (16), 813–820 DOI: 10.1364/OE.24.018468.

(16) Kruk, S.; Hopkins, B.; Kravchenko, I. I.; Miroshnichenko, A.; Neshev, D. N.; Kivshar, Y. S. Invited Article: Broadband Highly Efficient Dielectric Metadevices for Polarization Control. *APL Photonics* **2016**, *1* (30801), 1–9 DOI: 10.1063/1.4949007.

(17) Khorasaninejad, M.; Zhu, A. Y.; Roques-Carmes, C.; Chen, W. T.; Oh, J.; Mishra, I.; Devlin, R. C.; Capasso, F. Polarization-Insensitive Metalenses at Visible Wavelengths. *Nano Lett.* **2016**, *16*, 7229–7234 DOI: 10.1021/acs.nanolett.6b03626.

(18) Zhu, A. Y.; Kuznetsov, A. I.; Luk'Yanchuk, B.; Engheta, N.; Genevet, P. Traditional and Emerging Materials for Optical Metasurfaces. *Nanophotonics* **2017**, *6*, 452–471 DOI: 10.1515/nanoph-2016-0032.

(19) Staude, I.; Miroshnichenko, A. E.; Decker, M.; Fofang, N. T.; Liu, S.; Gonzales, E.; Dominguez, J.; Luk, T. S.; Neshev, D. N.; Brener, I.; Kivshar, Y. Tailoring Directional Scattering through Magnetic and Electric Resonances in Subwavelength Silicon Nanodisks. *ACS Nano* **2013**, *7* (9), 7824–7832 DOI: 10.1021/nn402736f.

(20) Decker, M.; Staude, I.; Falkner, M.; Dominguez, J.; Neshev, D. N.; Brener, I.; Pertsch, T.; Kivshar, Y. S. High-Efficiency Dielectric Huygens' Surfaces. *Adv. Opt. Mater.* **2015**, *3* (6), 813–820 DOI: 10.1002/adom.201400584.

(21) Zou, L.; Withayachumnankul, W.; Shah, C. M.; Mitchell, A.; Bhaskaran, M.; Sriram, S.; Fumeaux, C. Dielectric Resonator Nanoantennas at Visible Frequencies. *Opt. Express* **2013**, *21*, 1344–1352 DOI: 10.1364/OE.21.001344.

(22) Krasnok, A. E.; Miroshnichenko, A. E.; Belov, P. A.; Kivshar, Y. S. All-Dielectric Optical Nanoantennas. *Opt. Express* **2012**, *20* (18), 20599–20604 DOI: 10.1063/1.4750083.

(23) Zhao, W.; Jiang, H.; Liu, B.; Song, J.; Jiang, Y.; Tang, C.; Li, J. Dielectric Huygens' Metasurface for High-Efficiency Hologram Operating in Transmission Mode. *Sci. Rep.* **2016**, *6* (30613), 1–7 DOI: 10.1038/srep30613.

(24) Chong, K. E.; Wang, L.; Staude, I.; James, A. R.; Dominguez, J.; Liu, S.; Subramania, G. S.; Decker, M.; Neshev, D. N.; Brener, I.; Kivshar, Y. S. Efficient Polarization-Insensitive Complex Wavefront Control Using Huygens' Metasurfaces Based on Dielectric Resonant Meta-Atoms. *ACS Photonics* **2016**, *3*, 514–519 DOI: 10.1021/acsphotonics.5b00678.

(25) Yu, Y. F.; Zhu, A. Y.; Paniagua-Domínguez, R.; Fu, Y. H.; Luk'yanchuk, B.; Kuznetsov, A. I. High-Transmission Dielectric Metasurface with 2π Phase Control at Visible Wavelengths. *Laser Photonics Rev.* **2015**, *9* (4), 412–418 DOI: 10.1002/lpor.201500041.

(26) Shalaev, M. I.; Sun, J.; Tsukernik, A.; Pandey, A.; Nikolskiy, K.; Litchinitser, N. M. High-Efficiency All-Dielectric Metasurfaces for Ultracompact Beam Manipulation in Transmission Mode. *Nano Lett.* **2015**, *15*, 6261–6266 DOI: 10.1021/acs.nanolett.5b02926.

(27) Yu, N.; Genevet, P.; Aieta, F.; Kats, M. A.; Blanchard, R.; Aoust, G.; Tetienne, J.; Gaburro, Z.; Capasso, F. Flat Optics : Controlling Wavefronts with Optical Antenna Metasurfaces. *IEEE J. Sel. Top. Quantum Electron.* **2013**, *19* (3) DOI:

10.1109/JSTQE.2013.2241399.

(28) Bontempi, N.; Chong, K. E.; Orton, H. W.; Staude, I.; Choi, D.-Y.; Alessandri, I.; Kivshar, Y. S.; Neshev, D. N. Highly Sensitive Biosensors Based on All-Dielectric Nanoresonators. *Nanoscale* **2017**, *9*, 4972–4980 DOI: 10.1039/C6NR07904K.

(29) Yavas, O.; Svedendahl, M.; Dobosz, P.; Sanz, V.; Quidant, R. On-a-Chip Biosensing Based on All-Dielectric Nanoresonators. *Nano Lett.* **2017**, *17* (7), 4421–4426 DOI: 10.1021/acs.nanolett.7b01518.

(30) Komar, A.; Fang, Z.; Bohn, J.; Sautter, J.; Decker, M.; Miroshnichenko, A.; Pertsch, T.; Brener, I.; Kivshar, Y. S.; Staude, I.; Neshev, D. N. Electrically Tunable All-Dielectric Optical Metasurfaces Based on Liquid Crystals. *Appl. Phys. Lett.* **2017**, *110*, 1–4 DOI: 10.1063/1.4976504.

(31) Sautter, J.; Staude, I.; Decker, M.; Rusak, E.; Neshev, D. N.; Brener, I.; Kivshar, Y. S. Active Tuning of All-Dielectric Metasurfaces. *ACS Nano* **2015**, *9* (4), 4308–4315 DOI: 10.1021/acsnano.5b00723.

(32) Gutruf, P.; Zou, C.; Withayachumnankul, W.; Bhaskaran, M.; Sriram, S.; Fumeaux, C. Mechanically Tunable Dielectric Resonator Metasurfaces at Visible Frequencies. *ACS Nano* **2016**, *10*, 133–141 DOI: 10.1021/acsnano.5b05954.

(33) Aieta, F.; Kabiri, A.; Genevet, P.; Yu, N.; Kats, M. A.; Gaburro, Z.; Capasso, F. Reflection and Refraction of Light from Metasurfaces with Phase Discontinuities. *J. Nanophotonics* **2012**, *6*, 1–9 DOI: 10.1117/1.

(34) Nelder, J. A.; Mead, R. A Simplex Method for Function Minimization. *Comput. J.* **1965**, *7*

(4), 308–313 DOI: 10.1093/comjnl/7.4.308.

(35) Kivshar, Y.; Miroshnichenko, A. Meta- Optics with Mie Resonances. *Opt. Photonics News* **2017**, *28* (1), 24–31 DOI: 10.1364/opn.28.1.000024.

(36) Estakhri, N. M.; Alù, A. Recent Progress in Gradient Metasurfaces. *J. Opt. Soc. Am. B* **2016**, *33* (2), A21–A30 DOI: 10.1364/JOSAB.33.000A21.

(37) Kuznetsov, A. I.; Miroshnichenko, A. E.; Brongersma, M. L.; Kivshar, Y. S.; Luk'yanchuk, B. Optically Resonant Dielectric Nanostructures. *Science (80-.).* **2016**, *354* (6314), 1–9 DOI: 10.1126/science.aag2472.

(38) Lalanne, P.; Chavel, P. Metalenses at Visible Wavelengths: Past, Present, Perspectives. *Laser Photonics Rev.* **2017**, *11* (3), 1–11 DOI: 10.1002/lpor.201600295.

(39) Stulen, R. H.; Sweeney, D. W. Extreme Ultraviolet Lithography. *IEEE J. Quantum Electron.* **1999**, *35* (5), 694–699 DOI: 10.1109/3.760315.

(40) Chou, S. Y.; Krauss, P. R.; Renstrom, P. J. Imprint Lithography with 25-Nanometer Resolution. *Science (80-.).* **1996**, *272* (5258), 85–87 DOI: 10.1126/science.272.5258.85.

(41) Cord, B.; Lutkenhaus, J.; Berggren, K. K. Optimal Temperature for Development of Poly(methylmethacrylate). *J. Vac. Sci. Technol. B Microelectron. Nanom. Struct.* **2007**, *25* (6), 2013–2016 DOI: 10.1116/1.2799978.

(42) Henry, M. D.; Walavalkar, S.; Homyk, A.; Scherer, A. Alumina Etch Masks for Fabrication of High-Aspect-Ratio Silicon Micropillars and Nanopillars. *Nanotechnology* **2009**, *20*, 1–4 DOI: 10.1088/0957-4484/20/25/255305.

(43) Arbabi, A.; Arbabi, E.; Kamali, S. M.; Horie, Y.; Han, S.; Faraon, A. Miniature Optical Planar Camera Based on a Wide-Angle Metasurface Doublet Corrected for Monochromatic Aberrations. *Nat. Commun.* **2016**, *7*, 1–9 DOI: 10.1038/ncomms13682.

(44) Kamali, S. M.; Arbabi, E.; Arbabi, A.; Horie, Y.; Faraon, A. Highly Tunable Elastic Dielectric Metasurface Lenses. *Laser Photon. Rev.* **2016**, *10* (6), 1002–1008 DOI: 10.1002/lpor.201600144.

(45) Polman, A.; Atwater, H. A. Photonic Design Principles for Ultrahigh-Efficiency Photovoltaics. *Nat. Mater.* **2012**, *11*, 174–177 DOI: 10.1038/nmat3263.

(46) Wang, P.; Dominguez-Caballero, J. A.; Friedman, D. J.; Menon, R. A New Class of Multi-Bandgap High-Efficiency Photovoltaics Enabled by Broadband Diffractive Optics. *Prog. Photovoltaics Res. Appl.* **2015**, *23* (9), 1073–1079 DOI: 10.1002/pip.2516.

(47) Iyer, P. P.; Butakov, N. A.; Schuller, J. A. Reconfigurable Semiconductor Phased-Array Metasurfaces. *ACS Photonics* **2015**, *2*, 1077−1084 DOI: 10.1021/acsphotonics.5b00132.

For Table of Contents/Abstract Use Only:

High Efficiency All-Dielectric Huygens Metasurfaces from the Ultraviolet to the Infrared

Adam J. Ollanik*[*,†], Jake A. Smith[†], Mason J. Belue[†,‡], Matthew D. Escarra[†]

Computational and experimental results are presented for dielectric Huygens metasurfaces demonstrating highly efficient (91% computational, 64% experimental) anomalous refraction. Metasurfaces are demonstrated for ultraviolet, visible, and infrared wavelengths. A spectrum splitting device is also modeled; sensitivities of the metasurface system are discussed, along with prospective applications. The graphic shows (left) three metasurfaces demonstrating anomalous refraction in the ultraviolet, visible, and near-infrared, (right) SEM image of a fabricated metasurface, and (inset) diagram of the modeled spectrum splitting multi-layer device.